9-6-2021

Underground Burning of Jharia Coal Mine (India) and Associated Surface Deformation Using InSAR Data

Jungrack Kim

Shih-Yuan Lin

Ramesh P. Singh

Chen-Wei Lan

Hye-Won Yun

Underground Burning of Jharia Coal Mine (India) and Associated Surface Deformation Using InSAR Data

International Journal of Applied Earth Observations and Geoinformation 103 (2021) 102524

Contents lists available at ScienceDirect

International Journal of Applied Earth Observations and Geoinformation

journal homepage: www.elsevier.com/locate/jag

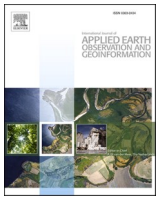

Underground burning of Jharia coal mine (India) and associated surface deformation using InSAR data

Jungrack Kim [a], Shih-Yuan Lin [b], Ramesh P. Singh [c,*], Chen-Wei Lan [d], Hye-Won Yun [e]

[a] RSS Hydro Research and Education Department, RSS-Hydro, Dudelange, Luxembourg
[b] Department of Land Economics, National Chengchi University, No.64, Sec. 2, Zhinan Rd., Wenshan Dist., Taipei City 116, Taiwan
[c] School of Life and Environmental Sciences, Schmid College of Science and Technology, Chapman University, Orange, CA, USA
[d] Disaster Prevention Technology Research Center, SINOTECH Engineering Consultants, INC., No. 280, Xinhu 2nd Rd., Neihu Dist., Taipei City 114, Taiwan
[e] National Disaster Management Research Institute, 365, Jongga-ro, Jung-gu, Ulsan 44538, Korea

ARTICLE INFO

Keywords:
Underground fire
Jharia coal mine
InSAR
Ground deformation
Thermal mapping

ABSTRACT

The underground burning in the Jharia coal mine (JCM) in India is a highly devastating environmental hazard inducing various adverse consequences. In the present study, we carried out time series analyses based on Interferometric Synthetic Aperture Radar (InSAR) and land surface temperature (LST) to study the environmental risk. First, a permanent scatterer (PS) time series analysis using Sentinel-1 images over three years was performed to detect the spatio-temporal distribution of ground deformation. Comparison of ground thermal anomaly clearly delineated the subsidence spots associated with the oxygen supply to combustion areas. On the contrary, few deformations were mapped showing pronounced uplift up to 10 mm/year compared with the horizontal creeping associated with underground fire activities. Such ground deformation and thermal anomaly patterns have never been observed. We modeled these observations from satellite data as a consequence of a strong pressurized source that induces surface migration in the coal mine and surrounding geological formations. Further, detailed investigations and modeling are required to mitigate the impact of hazards associated with the underground fires at different locations in the JCM.

1. Introduction

The destruction of the environment by a wide range of anthropogenic activities has become a common feature of socio-economic development. In particular, the strong desire to secure energy sources often leads to devastating environmental disasters in which residents suffer uncontrollable and unpredictable damages.

As part of an environmental catastrophe related to energy resources, the subject of this study is underground fires in coal mines. Automatic ignition of underground carbonate fuel reserves often occurs in large coal deposits due to natural ignition, such as lightening and wildfires, and can lead to large-scale underground fires. However, at present, several underground coal fires are triggered by anthropogenic factors, primarily unsupervised mining. These have become more destructive due to the surface fissure by mining activities, which serve as oxygen inlets and outlet ventilation paths (Kuenzer and Stracher, 2012).

The Jharia coal mine (JCM) is one of the most disaster-prone regions in India. Numerous accidents have occurred in the past that have impacted environment and loss of lives. JCM is considered as one of the important India's coal production mining areas, for producing high grade coking coal regions. However, JCM is well known for underground coal fires that have caused changes in topographic features and surface deformation, which are direct indicators of ongoing underground combustion. Many attempts have been made to utilize a variety of geophysical tools such as electrical resistivity (Bharti et al., 2016), numerical modeling (Singh and Yadav, 1995) and magnetic methods (Pal et al., 2016) to provide subsurface information and the areal extent of the burning coal. However, a complete reconstruction of the burning portion in sufficient spatio-temporal domains is not available from the in-situ observations. Thus, the remote sensing observations are considered as an appropriate approach for mapping of the burning coal mine areas.

In particular, InSAR techniques have been used to investigate the effects of surface deformation, hence are identified as a powerful tool to identify potential hazards and evaluate the associated damages. The InSAR signals integrated with Land Surface Temperature (LST) and

* Corresponding author.
E-mail address: rsingh@chapman.edu (R.P. Singh).

https://doi.org/10.1016/j.jag.2021.102524
Received 9 May 2021; Received in revised form 24 August 2021; Accepted 26 August 2021
Available online 6 September 2021

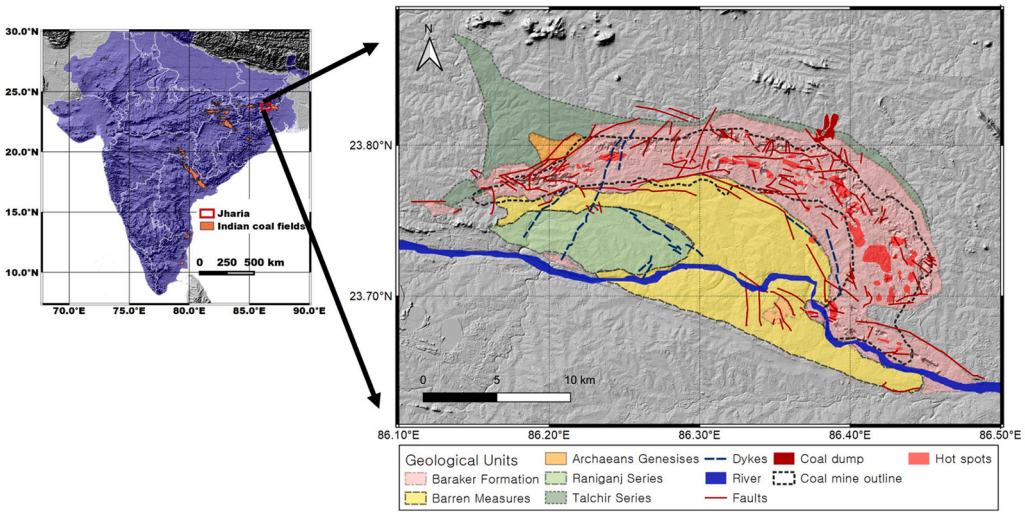

Fig. 1. Fig. 1 Location and geological context of the target area. Source: Bharat Coking Coal Limited (BCCL, 2008) report.

other spaceborne data were also employed in a few coal mine fire cases as shown in Srivastava et al. (2017), Wang et al. (2019a) and Riyas et al. (2021).

In this study, we analyzed InSAR data for the periods 2017–2020 and combined the results with the thermal anomaly by the means of geophysical model and correlation analyses to track underground coal mine fire in the JCM. The final results obtained from the synthesized analysis are promising to identify potential risk and develop further techniques to mitigate the impact of underground fire.

2. Study area and data

The extent of JCM covers 280 km^2 of Jharkhand State, the north-eastern province of India (Fig. 1). The coal fields are mainly distributed along the Damodar river valley and pass through multiple local cities whose economy mainly depend on the coal industry. Thus, the target area has been undergoing rapid industrial-urban development even with a significant environmental situation. The indispensable position of JCM for such local and national interests became a reason to prevent active policies that tackle coal mine disasters including underground fires.

The JCM underground fire was ignited in 1916 by an unidentified factor (BCCL, 2008) and has never extinguished in spite of huge efforts by the Indian government and local authorities. Since the first coal fire was detected in 1916, collapse due to underground fire has caused extensive subsidence and fissures that act as the suppling corridor of oxygen to sustain the underground fires. Thus, the JCM coal fires have existed for more than 100 years (BCCL, 2008) and numerous studies have been carried out to map the underground coal fires using satellite data (Martha et al., 2010; Chatterjee et al., 2010; Gangopadhyay et al., 2012). Recently, InSAR (Chatterjee et al., 2010; Gupta et al., 2014; Riyas et al., 2021), GPS and geophysical approaches (Chatterjee et al., 2016; Pal et al., 2016; Kumar and Pal, 2020) have been employed. Despite these efforts, the comprehensive shape of the underground burning fire in JCM still remains unclear. JCM consists of 23 underground and 9 open cast mining areas (Prakash et al., 2013). As per the data of the Bharat Coking Coal Limited (BCCL) total of 40 million tons of yearly coking coal production in JCM's mining veins, coal fire destroyed 37 million tons of coal and made 220 billion tons of coal inaccessible (Michalski, 2004).

The geological formation, including coal seam which lies on the Barakar Formation of Permian age (Verma et al., 1979), shows E–W and NW–SE strike dipping towards the center of the coalfield as shown in Fig. 1 (Vaish and Pal, 2016).

To address the issue, images both acquired by remote sensed SAR and thermal scanners were applied. Sentinel-1 SAR imagery featuring high spatiotemporal coverage over the JCM area was used. A total of 91 and 88 SAR images acquired respectively in ascending and descending modes over two years were introduced for time series analysis. The details of the images are listed in Table 1 and Supplementary F.1.

Table 1
Characteristics of employed Sentinel-1 images.

	Ascending mode	Descending mode
Image number	91	88
Master image	2018.12.102	2018.09.23
Time coverage	2017.03.17–2020.03.25	2017.03.1–2020.03.28.
Heading angle (deg)	−12.356	−167.622
Incidence angle (deg)	39.399	37.0026
Path	85	121
Frame	73	511
Acquisition time	12:20 GMT	00:11 GMT
Polarization	VV*+VH	

* VV polarization mode is for actual InSAR processing. Full connection graphs for PS analyses can be seen in supplementary F.1.

Regarding the surface temperature observation, we employed Moderate Resolution Imaging Spectroradiometer (MODIS) Land Surface Temperature and Emissivity (LST&E) product (MOD 21) and Landsat-8 Thermal Infrared Sensor (TIRS) (Jimenez-Munoz et al., 2009) data for mapping of thermal anomaly.

3. Methods

In order to map thermal anomalies and to study spatial distribution over the source area, we have used two LST products derived from satellite data. The monthly average MODIS LST&E product (MOD 21) derived using algorithm developed by Wan and Li (2008) have been used. The advantage of MOD 21 monthly products is the completeness of data coverage since the cloud gap was interpolated by the cloud free LST&E pixels for every month. In comparison to MODIS LST&E (500 m spatial resolution resampling/processed from 36 spectral channels with 250–1000 m resolutions), Landsat-8 TIRS with 100 m spatial resolution is optimal to obtain detailed thermal distribution and to identify localized thermal anomaly. For LST retrieval, we masked cloud cover using the QA pixel embedded in the level 1 Landsat-8 top of atmosphere (TOA) product prior to detailed analysis. The brightness temperature is calculated from well-known techniques as described in Jiménez-Muñoz et al. (2009) and Wang et al. (2019b).

The InSAR techniques have been used by many studies in the investigation of coal mine subsidence (Ge et al., 2007; Dong et al., 2013;

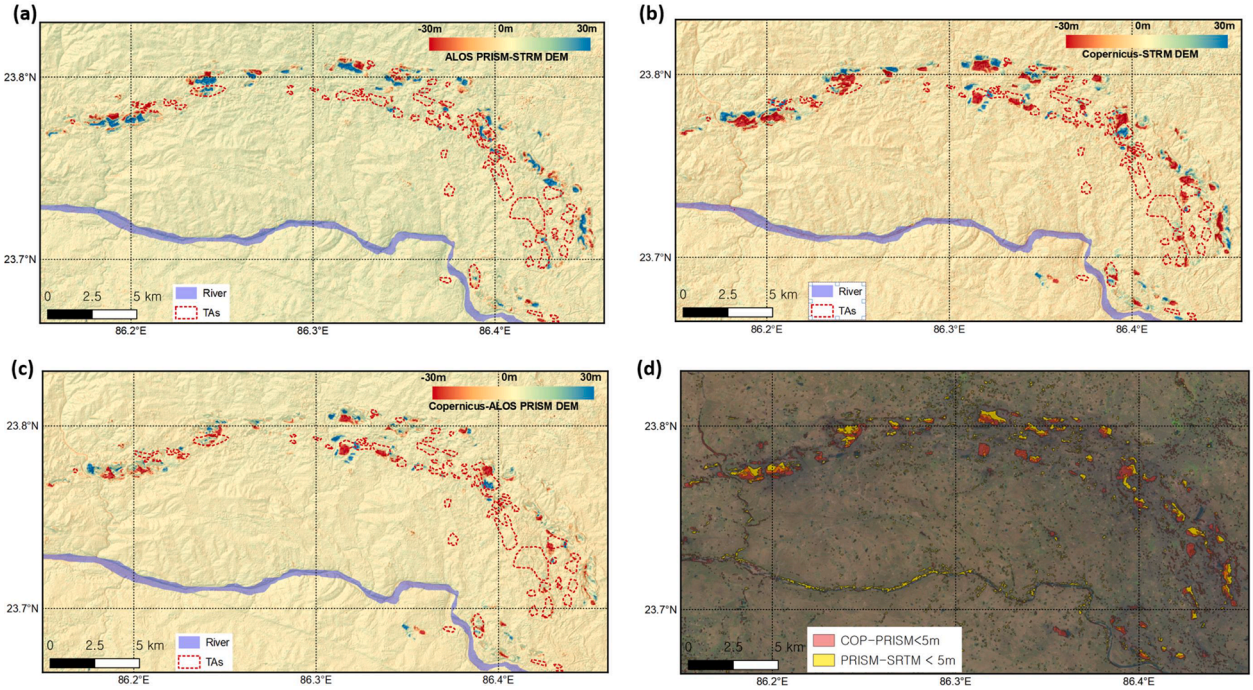

Fig. 2. Fig. 2 (a) ALOS PRISM vs. SRTM DEM residual, (b) Copernicus vs. ALOS PRISM DEM residual, (c) Copernicus vs. ALOS PRISM DEM residual, (d) Overlaid intensive surface mining areas by Copernicus-ALOS DEM and PRISM-SRTM DEM residual. TAs assigned by BCCL were plotted together.

Przyłucka et al., 2015). Theoretically, the InSAR accuracy for measuring surface deformation is capable of achieving a few millimeters (Gabriel et al., 1989). However, numerous components, such as base DEM error (European Space Agency, 2015), unregulated orbital information and the change of atmospheric condition, interfere with precise monitoring in practical applications. To address such various error components, time series analysis adopting multiple interferogram stacks together with processing algorithms is able to reduce error terms. According to the InSAR pair connection methods, the InSAR time series technique can be classified into Permanent Scatterer (PS) (Ferretti et al., 2001) and Small Baseline Subsets (SBAS) (Berardino et al., 2002). The temporal and spatial baseline conditions between SAR images in this study were adequate to adopt ordinary PS algorithms.

However, there is an issue regarding the temporal difference between the DEM used for InSAR processing and image acquisition because of the constantly changing topography of the target area caused by mining activity. We employed three DEMs, including the ALOS Panchromatic Remote-sensing Instrument for Stereo Mapping (PRISM) DEM extracted from a 2005–2010 stereo mission (Tadono et al., 2014), the Copernicus DEM (ESA, 2019) generated by the X-band InSAR mission over 2010–2015, and the SRTM DEM produced by the single-pass InSAR mission of 2000, to create DEM residuals (as shown in Fig. 2). Along with the mining activity in the mid-south area of JCM during the period conducted by BCCL (see Fig. 2(b)), constant cavities and deposits of up to +/- 30 m are shown by Copernicus and ALOS DEMs vs. SRTM DEM residual (Figs. 2(a) and 2(c)). It is noted that such high deformation areas up to a few meters per year do not fit well with the BCCL thermal anomalies (TAs) (Fig. 2). Considering source data acquisition times for DEMs, the Copernicus-ALOS DEM residual has presented surface mining activities since 2010. On the contrary, PRISM-SRTM DEM residuals are attributed to the surface mining activities during the periods 2000–2010. Our results show that the mining activities rapidly moved from southward existing mining places in JCM since mid-2000 (Fig. 2(d)).

Neither SBAS nor PS is an ideal approach to detect such a large scale deformation up to meter-scale per year because an area with such a large deformation cannot include any object that has consistently strong phase coherence. Consequently, PS as well as SBAS time series analyses would fail. Thus, our InSAR time series analysis concentrated on the area where the deformations are carried out by small surface creep originating from underground thermal activities. The magnitude would be at a rate of a few millimeters per year, which is most acceptable for PS analysis. It was known that PS is supposedly the most optimal approach to detect such small surface creeping generally observed over some artificial structures and rocky surfaces. The area with significant deformation associated with the mining activities or surface collapse, even with meter-scale were observed and interpreted by DEM residuals.

Based on the accuracy examination (Grohmann, 2018; Yun et al., 2019), we adopted ALOS PRISM DEM, a global 30 m resolution DEM (Takaku et al., 2018), as the base DEM of InSAR processing. It is worthwhile noting that mining activities in JCM changed the terrain steadily and extensively, thus expanding the errors of the old base DEM such as SRTM DEM.

The core idea of PS algorithm is to discriminate persistent scatterers with constant responses for amplitude dispersion and to address the error estimation using iterative non-linear equations. The density of extracted observations by PS processing was not optimal over the coal mine area in three years of time. Therefore, we made an additional effort to solve the trade-off problem between the density and reliability of scatterers by checking multiple PS results of the different threshold values in amplitude stability index (ASI) as.

$$\mathrm{ASI} = 1 - \frac{\sigma_A}{Stdev_A} \tag{1}$$

where m_A is the mean deviation of amplitude and $Stdev_A$ is the standard deviation of amplitude in time domain. PS points with ASI > 0.75 were selected first and estimated for the deformation model. Based on the adjustment model residual, each slave image's atmospheric phase screen (APS) respected to master image was retrieved and then subtracted from each interferogram. After APS is eliminated, lower ASI was applied to increase number of PS points and to make a final estimation to establish the velocity map. It was noted that high ASI PS point network was not feasible over significant topographic changes induced by surface mining activities. The minor changes on topography could be

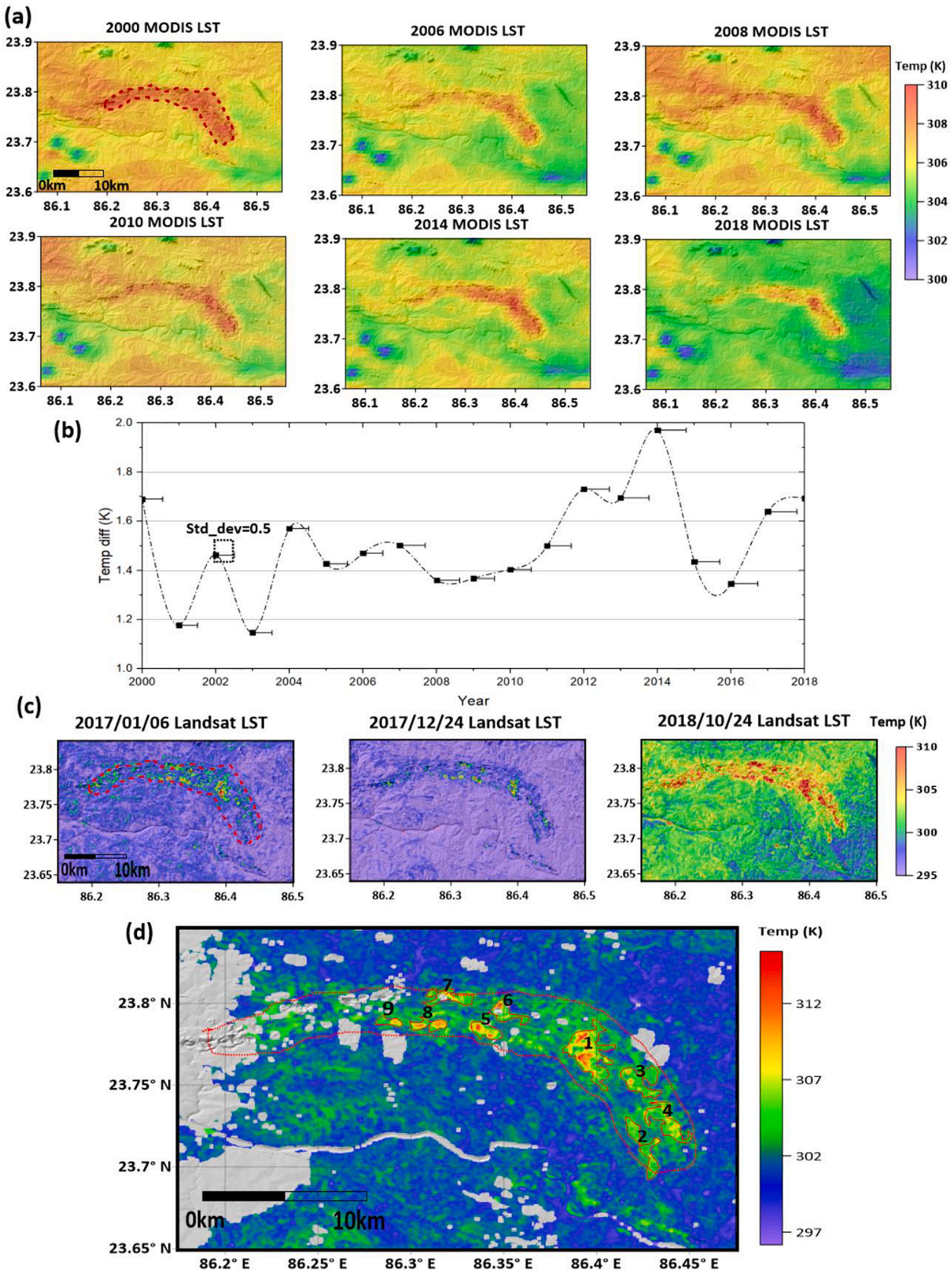

Fig. 3. Fig. 3 (a) Samples of MODIS MOD 11 yearly average LST (see supplementary F.2 for the other LST samples.) and (b) the trend of MODIS yearly mean TD, i.e., temperature difference between HTI (see red dotted line in a) compared to surrounding background. (c) Some samples of Landsat-8 LST (d) TAs detection (named as TA1-TA9) from mean Landsat-8 temperature (TD > 3 degree). (For interpretation of the references to colour in this figure legend, the reader is referred to the web version of this article.)

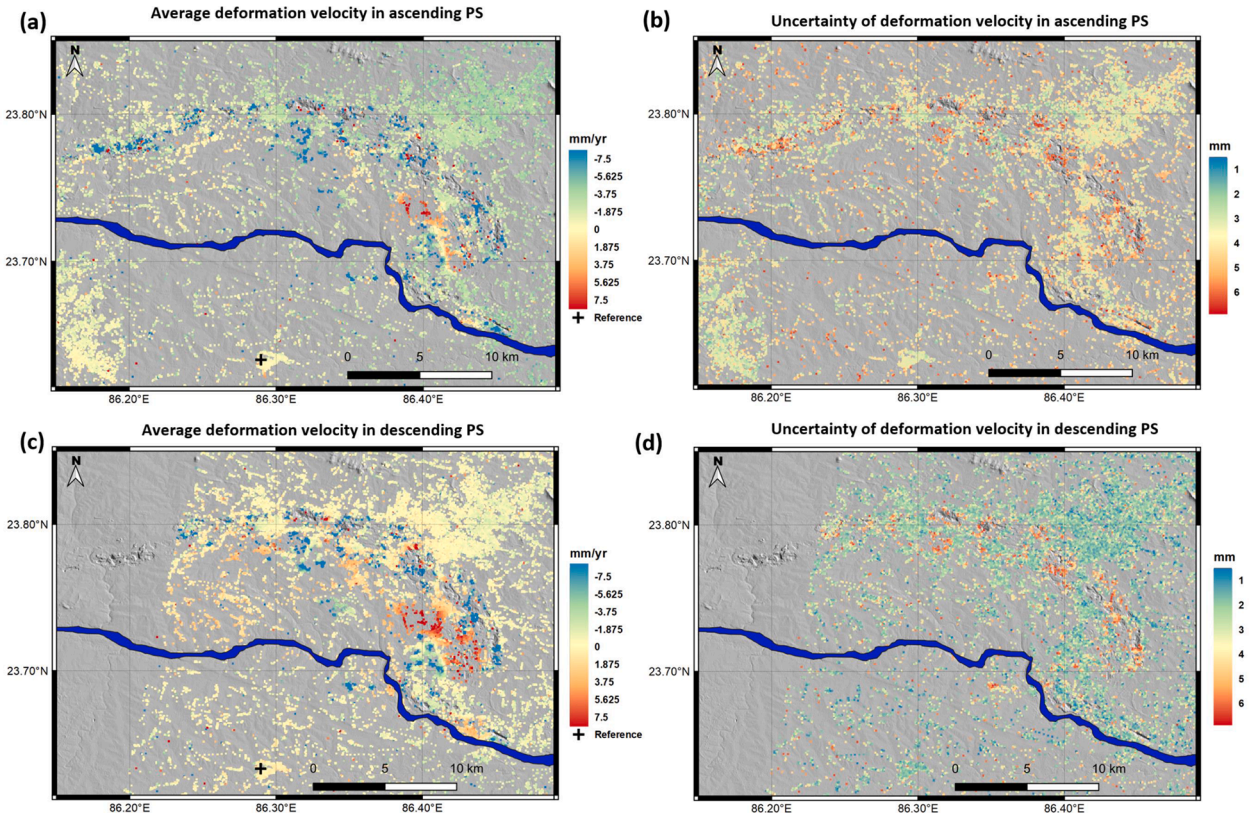

Fig. 4. Fig. 4 (a) LOS deformation velocity by descending mode PS InSAR time series analysis during April 2017 to March 2020, (b) Uncertainty of deformation velocity of descending mode processing, (c) LOS deformation velocity by descending mode PS InSAR time series analysis during April 2017 to March 2020, (d) Uncertainty of deformation velocity of ascending mode processing.

compensated by error correction routine of iterative non-linear equations in PS processing. However, further introduction of distributed point (DS) to increase point density is not possible as the algorithmic bases of DS lacks of base DEM errors compensation that was a strong requirement in our target area, especially around surface mining areas presented in Fig. 2.

The LOS deformations using PS InSAR is related to image acquisition conditions such as incidence and azimuth angles. Only once a decomposition based on the ascending and descending InSAR deformations was performed, horizontal and vertical migrations could be derived. Then, a quantitative interpretation in terms of thermal response with corresponding topography could be implemented correctly to minimize the effect of topography. We have considered 88 descending mode InSAR observations which were interpolated at the acquisition times of the ascending mode InSAR pairs. Mathematically the interpolation procedure utilized a least squares quadratic equation fit with a 2nd order polynomial function together with a spatial adaptive filter to fill the spatial gap (Yun et al., 2019). In order to achieve actual decomposition, we introduced the relationship by Fialko et al. (2001) as

$$\begin{pmatrix} \frac{dispA}{dispD} \end{pmatrix} = \begin{pmatrix} -sin\theta_{asc}cos\alpha_{asc} & cos\theta_{asc} \\ -sin\theta_{desc}cos\alpha_{desc} & cos\theta_{desc} \end{pmatrix} \begin{pmatrix} \frac{dispH}{dispV} \end{pmatrix} \quad (2)$$

where *dispA* is LOS deformation in ascending mode observation, *dispD* is LOS deformation in descending mode, *dispH,* and *dispV* are horizontal and vertical deformations, θ_{asc} and θ_{desc} represent the incidence angles of the ascending and descending mode observations and α_{asc} and α_{desc} are the heading angles of the ascending and descending modes. For model inversion of pressurizing source caused by coal fires, we used the Geodetic Bayesian Inversion Software (GBIS) tool (Bagnardi and Hooper, 2018) which is capable of parameter inversion in deformation source based on Markov-chain Monte Carlo methods and the Metropolis-Hastings algorithm.

4. Results

4.1. Mapping of land surface temperature

Fig. 3(a) shows the subset of monthly averaged MODIS MOD 21 over the study area. Although no detailed thermal anomalies are observed from MODIS MOD 21 products directly, the hot thermal island (HTI, outlined by the red dotted polygon in Fig. 3(a)) is extracted from Principal Component Analysis (PCA) using MODIS MOD 21 data stack for 18 years with further processing (Fig. 3(b)). On the contrary, Landsat-8 LST (Fig. 3(c)) shows a distribution of thermal anomalies related to underground coal mining burning areas. Upon the carefully established 44 cloud free Landsat-8 LST time series for the periods 2017–2020, we have observed continuous TAs over the JCM as shown in Fig. 3(c) and 3(d). The strong thermal anomaly (10 degrees higher than non-coal mine area) is closely related to the eastern part of JCM area. For further analyses, we employed the temporal residual between LST of TAs and HTI compared to the surrounding non-coal mine area, referred to as "Temperature difference (TD)" which was less dependent on seasonal and long-term climatic conditions. Fig. 3(b) shows the trend of TD change over HTI for the past two decades. The trend is not clear. However, the standard deviation of TD in HTI is found to be increasing. It was noted that TAs in Fig. 3(d) were defined as TD $>$ 3 degree areas. Based on that, the detailed analysis of TAs is further discussed in view of the surface deformations observed from InSAR data.

4.2. Mapping of land surface deformation

Fig. 4 shows the Line of Sight (LOS) deformations extracted from InSAR PS time series analysis over the JCM area together with their uncertainties (Fattahi and Amelung, 2015). The time series of the LOS surface deformation map (Fig. 4) shows that the surface deformations

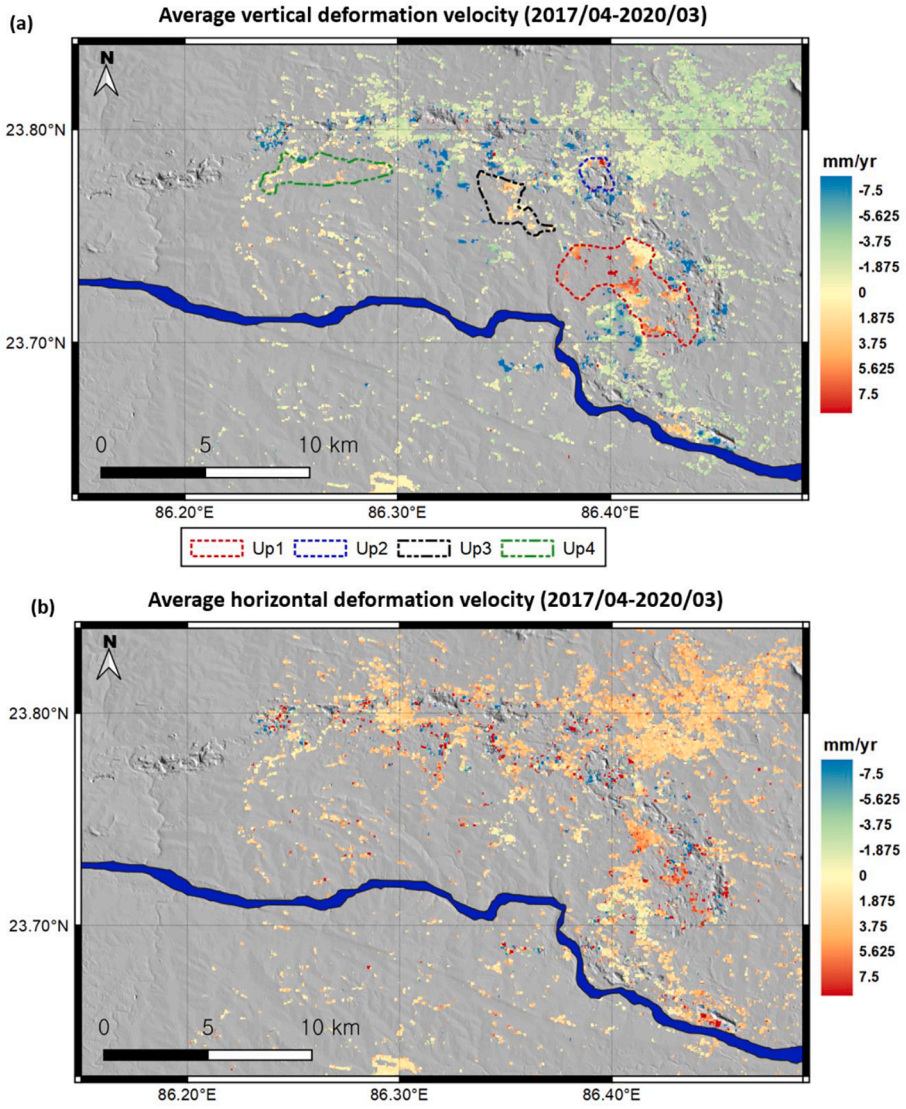

Fig. 5. Fig. 5 (a) Average vertical and (b) horizontal velocities by decomposition. Dotted parts are the identified uplift regions and designated Up1-4 for further interpretation.

over the study area can be classed into different sub-regions. In particular, there was a discrepancy in the JCM HTI and surface deformation in ascending and descending modes over the eastern part of the JCM, showing strong thermal anomaly. Therefore, the precise patterns in horizontal and vertical directions and their correlation with the LST distribution should be analyzed accordingly based on the decomposed LOS deformations in ascending and descending modes. A migration of velocity of a few millimeters per year in the northeastern side of JCM centered on Dhanbad city area was noticed, perhaps because of either surface creep along E-W directional segmented faults or unresolved regional sources. As this is outside of HTI, it is not included as part of our interpretation.

5. Interpretation and discussion

Since the LOS InSAR observations, given in equation (2) were interpolated to be located in the same temporal interval, it is possible to solve equation (2) in order to decompose the vertical/horizontal deformations (Fig. 5). The deformation patterns show: 1) four obvious deformation areas with strong uplift and horizontal creeps (represented as Up1-4 in Fig. 5(a)); 2) sporadically populated vertical subsidence as stated in the following interpretations; and 3) vertical/horizontal migration patterns, perhaps associated with the behaviors of TAs (referred to Fig. 7).

The horizontal deformation extracted by the decomposition consists of the N–S and E–W directional deformations. In fact, the N-S component has smaller contributions to LOS measurement compared to the E-W component, as Sentinel-1 orbit is highly close to polar orbit (Hu et al., 2014). In other words, as long as N-S migration is not significantly greater than E-W, the N-S contribution to LOS is negligible (Fuhrmann and Garthwaite 2019). It must be noted that the contribution of E-W deformation to LOS observation is 4–5 times bigger than N-S deformation in the condition of this image acquisition presented in Table 1. Thus, the prevalence of N-S migration over major deformations in Up1 to Up4 is only possible with strike-slip fault geometry closely aligned with the N-S direction. Ground survey by BCCL (2008) (see Fig. 1) and other precedent studies did not identify any significant N-S directional faults and structural lineaments especially over thermal and migration anomalies. Thus, the probability of a stronger N-S migration compared to an E-W migration is likely far less. Particularly on the eastern migration anomaly defined as Up1, the detailed behavior (Fig. 6) shows a unique characteristic. Considering the shape of horizontal deformation patterns in the Up1 area (Fig. 6(b)) and a combustion mechanism inducing such horizontal migrations stated as follows, it is estimated

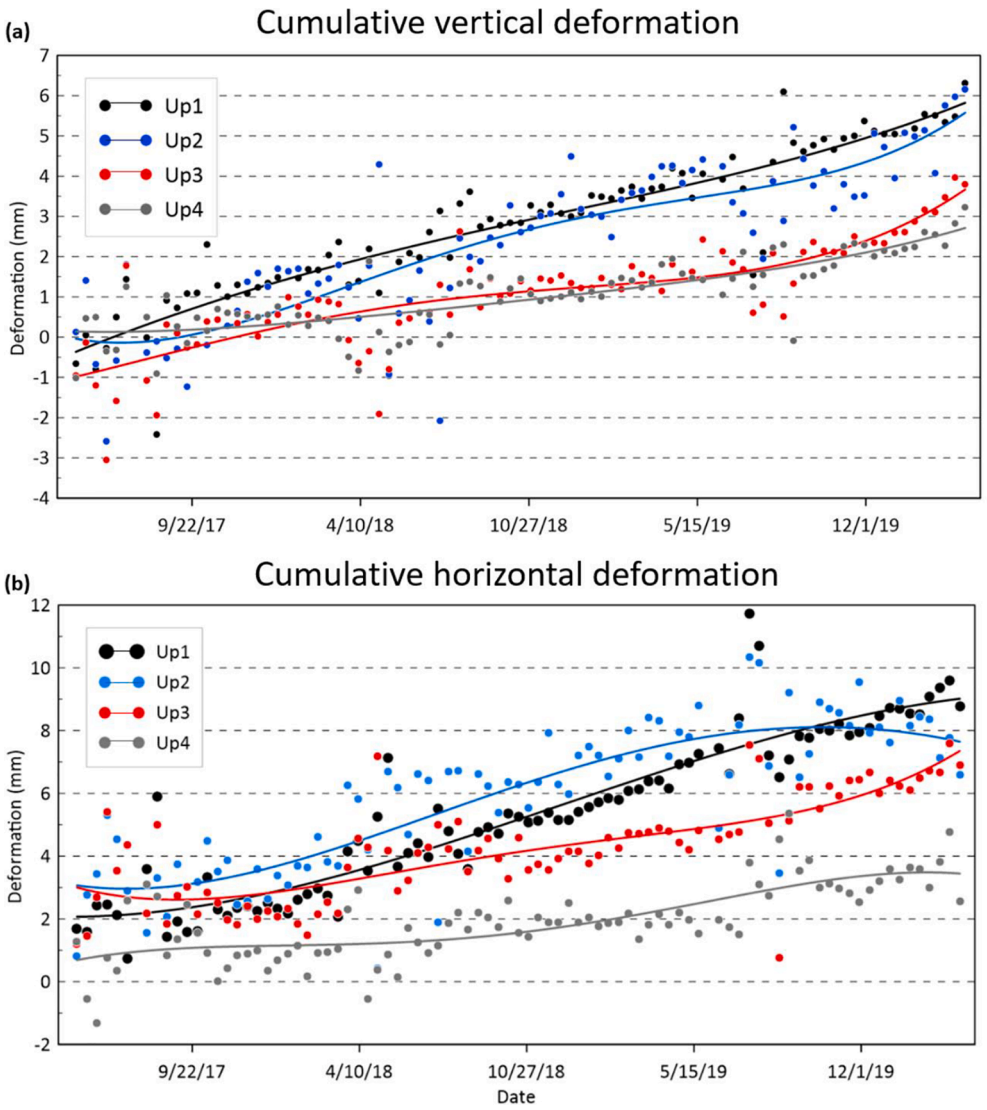

Fig. 6. Fig. 6 Time series observations of (a) cumulative vertical and (b) horizontal deformations over Up1-4.

that the horizontal migration could be directed in NNW-EES. Given the absence of anthropogenic changes in topography, such as debris dumping, the plausible exploration is instead the gradual migration of topography by a certain strain accumulation. The increasing pressure caused by combustion could be the source leading to the potential uplifting and NNW-EES directional horizontal creeping.

The Up3 and 4 show weaker vertical uplift and horizontal migration in different ways compared to Up1 (Fig. 7). Perhaps the horizontal creeping in Up2 is going through SEE to NNE direction considering the location of Up2 and horizontal migrations of InSAR observation (Fig. 6 (b)). It was noted that the results of the analysis summarized above are similar to the outcomes derived by finite element method as shown in Paul and Chatterjee (2011), especially in Up1 area. We hypothesized a certain connection between the thermal activities within HTI and the horizontal/vertical motions in Up1-4 and examined the temporal correlation as shown in Fig. 7. First, the TD and deformations within Up1-4 (refer to Fig. 7(a)) are not highly correlated even after removal of noisy components using average up to 30 days moving window size. Low correlation values in time series are not usable (see supplementary T.1). Thus, presumably the surface deformation in Up1-4 areas is developed by a certain mechanism other than combustion in direct drop subsurface.

The TDs in hotspots 1–9 observed from Fig. 3 appear to be correlated with the migration of Up1-4 (see Fig. 7(b) to 7(f)). In particular, the time lagged trend between TD and deformation pairs (TA 1 vs. Up1, TA 1 vs. Up2, TAs 2,3,4 vs. Up1 and TAs 5,6,7,8,9 vs. Up3,4) is observed. Around JCM areas, 77% of total yearly precipitation (1300 mm/year) occurs during the monsoon season (June - October) that may significantly affect the thermal behaviors of TAs and induce time lag horizontal/vertical deformations. Also, there is a 1–2 month of time lag response between horizontal and vertical deformations perhaps due to the different brittle reaction to external pressure.

The correlations between TDs and deformations were highly different to track as they are influenced by long term trends covering the whole observation period as well as the contributions from different pressure sources (supplementary T.1). Hence, we employed the cross-wavelet and coherence analysis (Torrence and Compo, 1998) as it is widely known as a highly robust approach to check the temporal correlation of complicated time series observations (Liu et al., 2007).

As shown in the cross wavelet analysis (referred to in Fig. 8), the TDs and vertical/horizontal deformations of all pairs (TA1 vs. Up1, Up1 vs. Up1, TA2,3,4 vs. Up1) are somehow correlated with a considerable time lag (< 80–270 days) and 10 to 30 day periodicities. On the other hand, the apparent strong correlations between the TD and the horizontal deformation velocities in TA1 vs. Up1 and TA2,3,4 vs. Up1 pairs are shown in the cross coherence wavelet analysis. For the effectiveness of

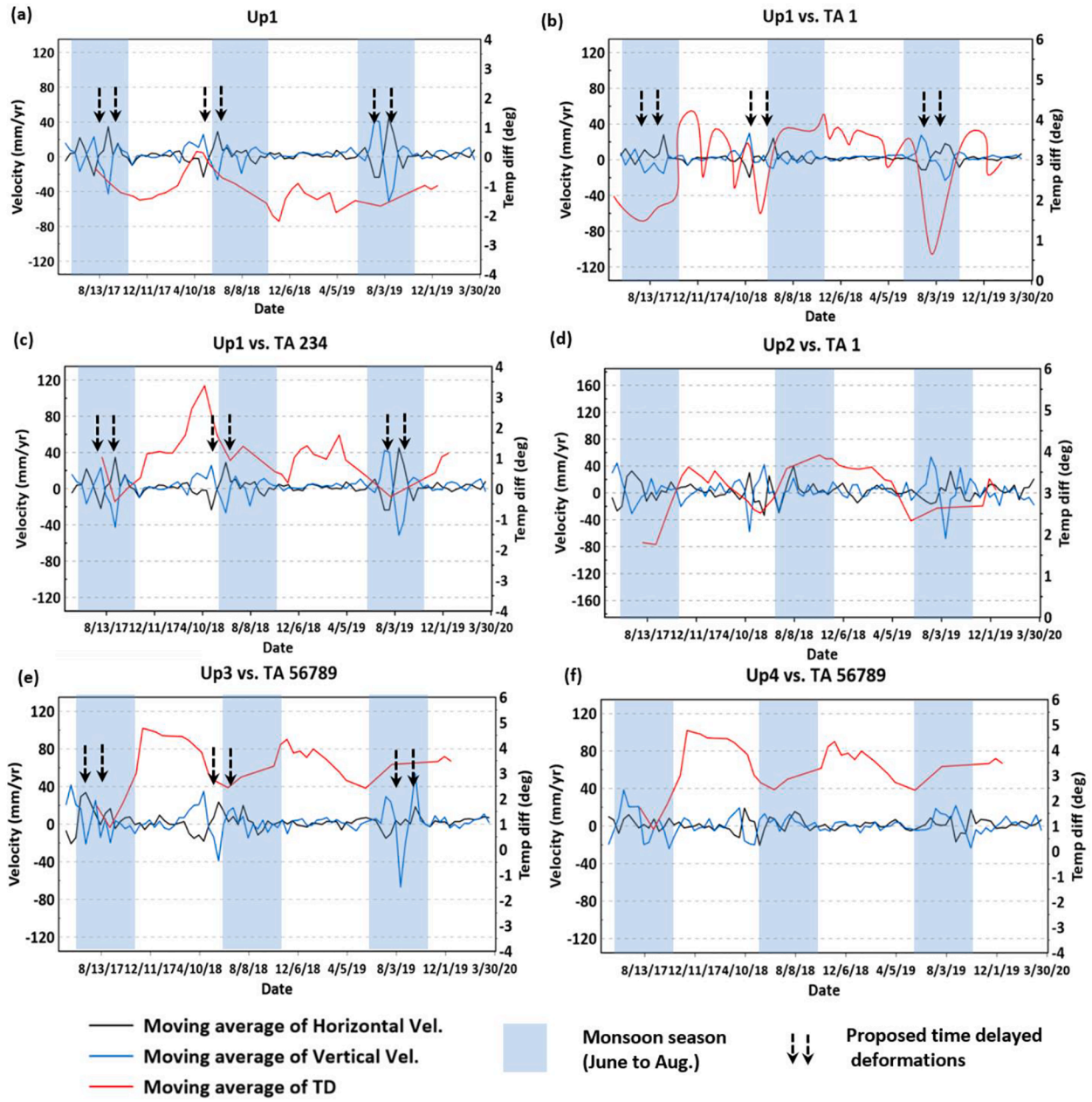

Fig. 7. Fig. 7 Time series observations of TD and vertical/horizontal deformations (a) deformation velocity in Up1 vs. TD in Up1, (b) Deformation velocity in Up1 vs. TD in TA1, (c) deformation velocity in Up1 vs. TD in TA2,3,4, (d) deformation velocity in Up2 vs. TD in TA1, (e) deformation velocity in Up3 vs. TD in Up56789, (f) deformation velocity in Up4 vs. TD in TA5,6,7,8,9. The assigned monsoon season compared to the significant changes in TD together with delayed deformation signals was noticed.

cross coherence wavelet analysis rather than cross wavelet analysis to observe a minor correlation(Jevrejeva et al. (2003). The correlation in the pair of TD of Up1-deformation of Up1 is not very clear (Fig. 8(a)). It was noted that the correlations between TDs over other TAs 2–9 and the deformation velocities of Up2-4 are very weak and unclear. Thus, their wavelet analyses were not presented herein. Based on these observations, we concluded that the deformations in Up1 and Up2 was involved with the underground combustion in the observed TA1 and 2,3,4.

The height residual and vertical subsidence points were considered in order to infer the combustion mechanism in TAs causing the surface deformations (Fig. 9(a)). We treated a negative value in height residual between Copernicus and ALOS PRISM DEMs as the representation of topographic change induced by surface mining and consequent collapses exhumed closely to the surface. As a result, surface mining areas were found over all around the TAs. For further interpretations, the distributions of ground subsidence points gained from InSAR vertical deformation (threshold < -2 mm/year) were introduced. The areas of large DEM residuals presented in Fig. 9(a) and the population of ground subsidence points do not overlap due to the decorrelation issue over large ground deformation areas. Moreover, all subsidence points identified by InSAR PS analysis were filled along lineaments that were connected through TAs, as shown in Fig. 9(a). Therefore, the best proposed model is that the oxygen supplying lineaments created by slow but steady ground subsidence could cause cracks and fissures on the surface, which are likely related to underground combustion areas of TAs. The heavy surface mining areas also supply oxygen to TAs. Therefore, the combustion chamber, especially in TA1 and 2,3,4, made the most obvious surface creeping in Up1 and Up2 centered in Jharia and Dhanbad regions. The artificial settlements, especially concentrated in Jharia areas (Fig. 9(b)), acted as an insulating cover from underneath

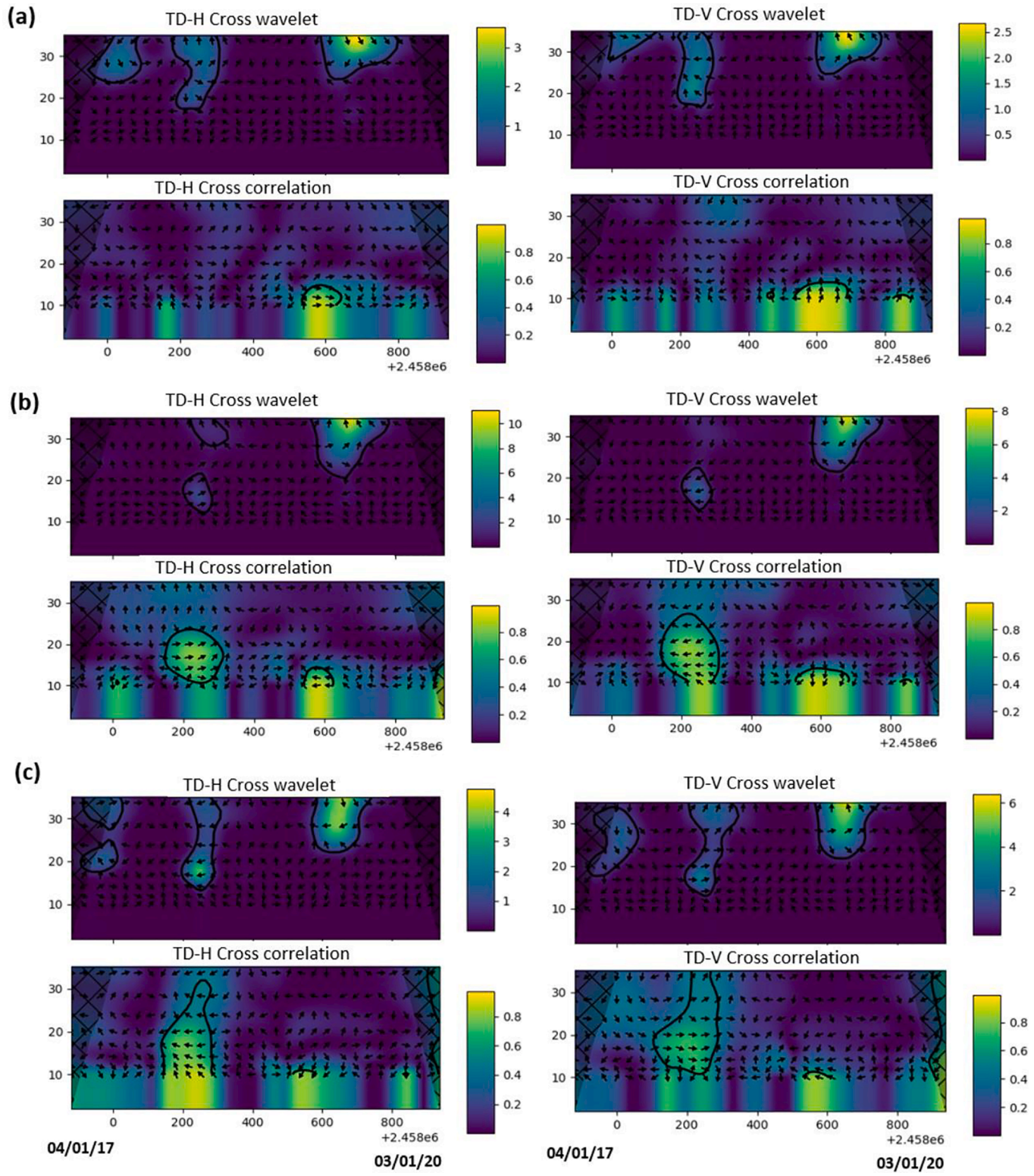

Fig. 8. Fig. 8 Cross wavelet and wavelet coherence analyses between TD and deformation. (a) TD in Up1 vs. deformations in Up1, (b) TD in TA1 vs. deformations in Up1 and (c) TD in TA2,3,4 vs. deformations in Up1. The shaded parts represent the outside of the influenced cone where edge effects may dominate. The black contours specify the 5% significant level against noises. Arrows indicate relative phase relationship; thus, it means the lag time between two independent observations.

burning coal fires and prevented the propagation of the fissure. Instead, this caused significant uplifting and horizontal creep on the Up1 and part of the Up2 by a certain mechanism of thermal and pressure sources.

The deformations in Up1 are much higher due to its upward/ horizontal strains caused by the closely connected TA1 and 2,3,4. The location and other parameters responsible in underground source of stress in Up1 can be more readily calculated by model inversion by GBIS due to the clear and strong deformation patterns (refer to Fig. 10 and

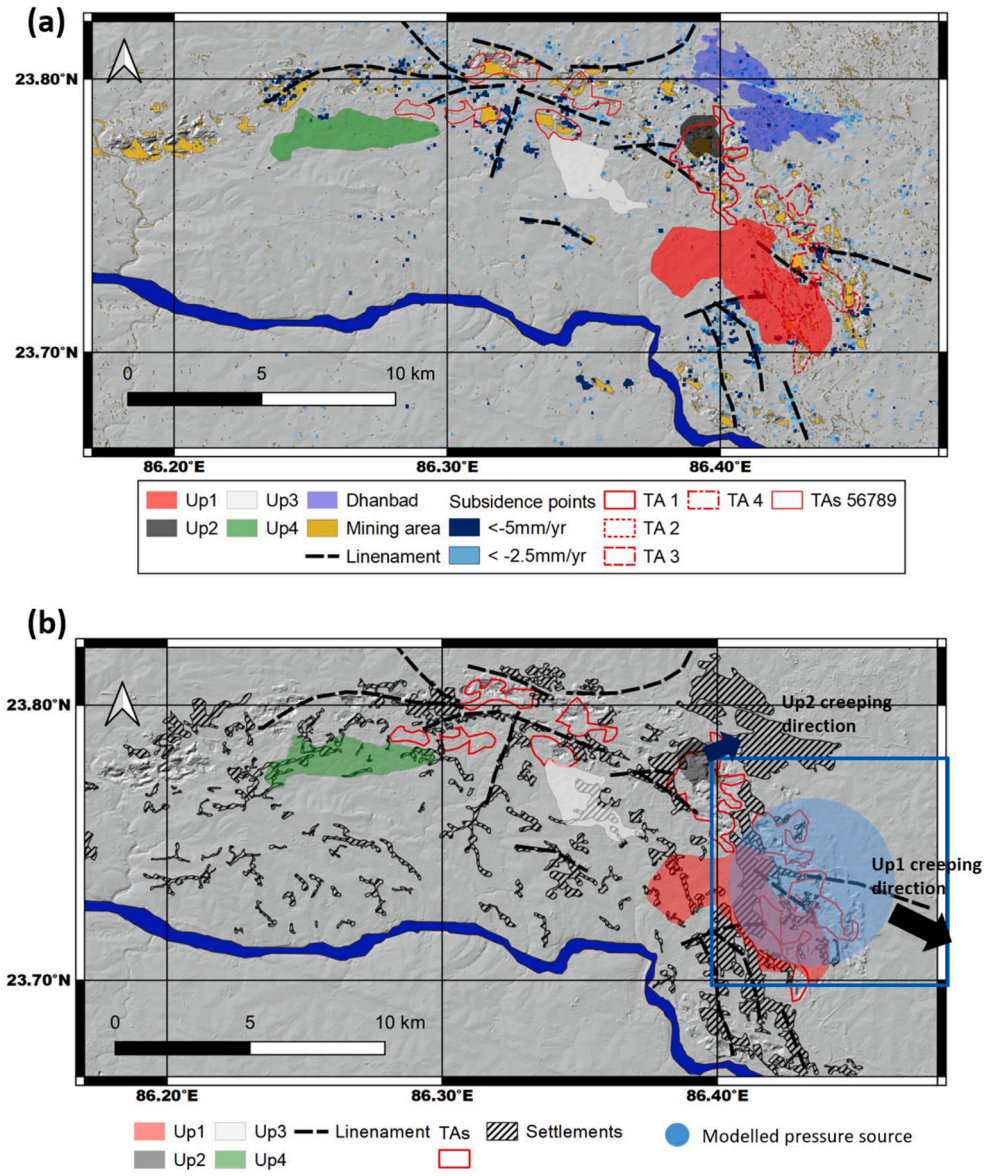

Fig. 9. (a) The distributions of ground subsidence points and the proposed lineaments. (b) The extent of GBIS modeling is given in box together with footprints of TAs and the settlements.

Table 2). Since the optimal model of pressure source in Up1 is Mogi type (Mogi, 1958), inducing circular deformation pattern (Fuhrmann and Garthwaite, 2019) and other source model like Okada type (Okada, 1985), that can induce N-S strike slip was failed, we confirm our hypothesis for prevailing E-W migration on deformation sources. However, the oxygen supplies composed of subsidence points and surface mining areas also caused the ceasing of combustions on the pressurizing sources in monsoon season as shown in Fig. 7. This induced sudden changes in vertical/horizontal deformations. It is proposed that the extensive but weak vertical migration over Dhanbad city area possesses a different deformation mechanism from the deformations in Up1-4 as there is no TA.

Discrepancies with precedent geodetic studies reported in Gupta et al. (2014) and Chatterjee et al. (2016) implying extensive and strong subsidence can be explained in the following ways. Two-pass InSAR analysis by Chatterjee et al. (2016) observed changes of the actual topography by mining activities, which are also presented in DEM residual analysis (Fig. 9(a)). It is not the subtle surface creeping detected in the PS analysis in this study. On the contrary, PS cannot be formed within undergoing mining areas and was mostly mapped by scatterers in artificial structures of residential and mining facilities. Due to the advantages of PS processing, the uplift/horizontal creeping areas were identified in this study but were not observed in earlier studies (Gupta et al., 2014; Chatterjee et al., 2016).

The behavior of uplift areas involving combustion processes was difficult to explain by only a single pressure source as the uplift areas are crossed connected by multiple TAs as shown in Fig. 8. The LOS deformations in Up1 and TA1 shown in Fig. 9(b) was applied by the GBIS model inversion to extract parameters given in Table 2. The modeled pressurizing source covered a considerable area and certainly was insulated by settlement over Jharia. However, the sources in Up2, Up3 and Up4 were difficult to establish model and were deduced as the comparable spatial extents of corresponding uplift areas based on the characteristics of Up1 source. Presumably, the deformation mechanisms of Up3 and Up4 are similar to Up1 but the combustions in TA5-TA7 are weaker and the insulation by human settlements are limited. Thus, relatively weak uplifting and horizontal creeps in Up3 and Up4 can be explained. The directions of horizontal creeping in Up1-4 plausibly E-W direction that induced from the information of decomposition and combustions. In future, we can follow enhanced InSAR error correction

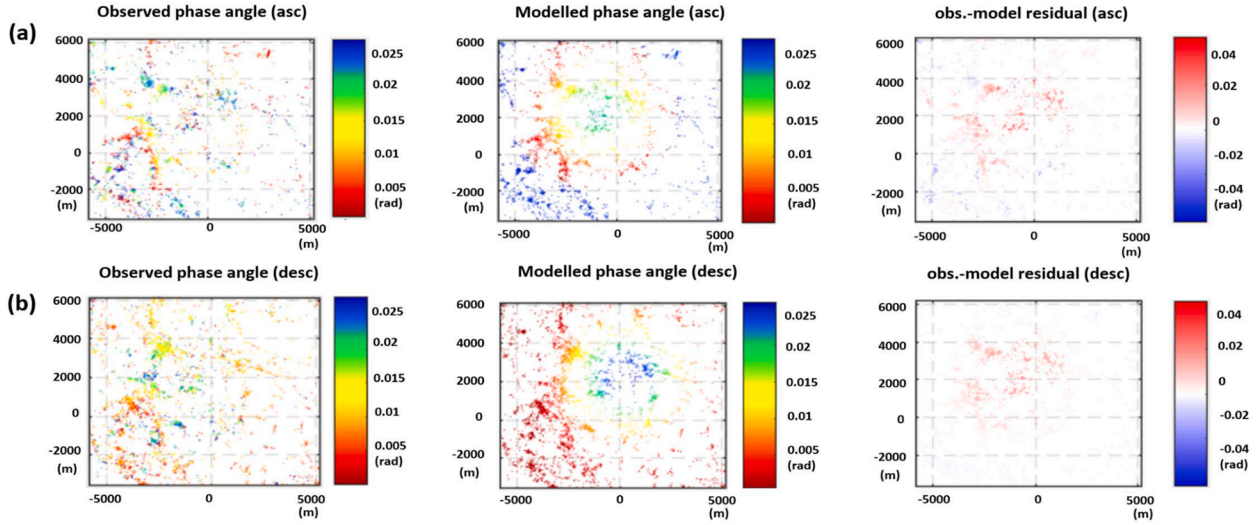

Fig. 10. Fig. 10. Observed and modeled deformation over Up1 employing GBIS inversion tools (a) Observed and modeled deformation in ascending InSAR together with residual between observations and model and (b) observed and modeled deformation in descending InSAR. The extent of GBIS is given in box in Fig. 9 (b).

Table 2
Inverted pressure source model in Up1 by GBIS.

Parameter	Optimal	Mean	Median
X coordinate	−269.64	−255.95	−259.58
Y coordinate	2299.97	1977.49	2163.77
Depth	1831.22	2572.30	2684.79
Radius	3361.06	2845.07	2789.96
DP/mu	5.313e-06	1.414e-05	1.138e-05

techniques proposed by Yunjun et al. (2019) that will provide better strain/pressure analysis to have better understanding of surface deformation in the JCM.

6. Conclusions

Using detailed analysis of satellite retrieved thermal anomaly and topographic deformation, we have discussed the possible mechanisms of ground deformation and thermal activities over JCM. The two major conclusions based on the present study are: 1) Combustion in TAs, especially in the eastern part of JCM, is the main driver of ongoing surface migration; and 2) the surface changes over JCM HTI consist of the chains of ground subsidence points and four major uplifting areas. Presumably, these surface deformations observed from the high precision PS approach were caused by interaction with thermal activities and the strain of topography. It should be discriminated from the rapid change of terrain induced by mining activity, which has been investigated from the precedent geodetic campaigns. In particular, the deformation in the Jharia city area can pose a great threat to weak residential building and mining facilities. Therefore, it is necessary to perform a constant monitoring to mitigate likely hazards. Based on the outcomes of this study, we strongly propose that the most significant concern of underground coal burning is the stability of artificial structures in the eastern part of JCM. In addition, it should be noted that cracks in residential areas due to the continuous strain can also pose a risk of toxic gas leakage. To better prepare for these potential hazards associated with the land, infrastructure and human health, high precision geodetic measurements can be planned accordingly.

CRediT authorship contribution statement

Jungrack Kim: Conceptualization, Methodology, Formal analysis, Data curation, Writing - original draft. **Shih-Yuan Lin:** Conceptualization, Methodology, Writing - review & editing. **Ramesh P. Singh:** Conceptualization, Methodology, Writing - review & editing. **Chen-Wei Lan:** Data curation, Formal analysis, Writing - review & editing. **Hye-Won Yun:** Data curation, Formal analysis.

Declaration of Competing Interest

The authors declare that they have no known competing financial interests or personal relationships that could have appeared to influence the work reported in this paper.

Acknowledgments

The paper contains Copernicus Sentinel data [2017-2018] processed by ESA. The authors acknowledge funding support by the Ministry of Science and Technology (MOST) in Taiwan under grant number MOST 110-2119-M-004-001. The authors are grateful to the Associate Editor and two anonymous Referees for providing detailed comments/suggestions which have helped us to improve earlier version of the manuscript.

Data availability statement.

The data that support the findings of this study are available from the corresponding author, and it will be available to all the interested readers.

[Ramesh P. Singh (rsingh@chapman.edu)], upon reasonable request.

Appendix A. Supplementary data

Supplementary data to this article can be found online at https://doi.org/10.1016/j.jag.2021.102524.

References

Bagnardi, M., Hooper, A., 2018. Inversion of surface deformation data for rapid estimates of source parameters and uncertainties: A Bayesian approach. Geochemistry. Geophys. Geosystems 19, 2194–2211.

BCCL (Bharat Coking Coal Limited), 2008. Master plan for dealing with fire, subsidence and rehabilitation in the leasehold of BCCL, in: Limited, B.C.C. (Ed.).

Berardino, P., Fornaro, G., Lanari, R., Sansosti, E., 2002. A new algorithm for surface deformation monitoring based on small baseline differential SAR interferograms. IEEE Trans. Geosci. Remote Sens. 40, 2375–2383.

Bharti, A.K., Pal, S., Priyam, P., Kumar, S., Srivastava, S., Yadav, P.K., 2016. Subsurface cavity detection over Patherdih colliery, Jharia Coalfield, India using electrical resistivity tomography. Environ. Earth Sci. 75, 443.

Chatterjee, R.S., Lakhera, R.C., Dadhwal, V.K., 2010. InSAR coherence and phase information for mapping environmental indicators of opencast coal mining: a case study in Jharia Coalfield, Jharkhand. India. Can. J. Remote Sens. 36, 361–373.
Chatterjee, R.S., Singh, K.B., Thapa, S., Kumar, D., 2016. The present status of subsiding land vulnerable to roof collapse in the Jharia Coalfield, India, as obtained from shorter temporal baseline C-band DInSAR by smaller spatial subset unwrapped phase profiling. Int. J. Remote Sens. 37, 176–190.
Dong, S., Yin, H., Yao, S., Zhang, F., 2013. Detecting surface subsidence in coal mining area based on DInSAR technique. J. Earth Syst. Sci. 24, 449–456.
European Space Agency, 2015. The Copernicus DEM from WorldDEM data, https://earth.esa.int/documents/700255/4038547/3+Leister+2.pdf.
Ferretti, A., Prati, C., Rocca, F., 2001. Permanent scatterers in SAR interferometry. IEEE Trans. Geosci. Remote Sens. 39, 8–20.
Fialko, Y., Simons, M., Agnew, D., 2001. The complete (3-D) surface displacement field in the epicentral area of the 1999 Mw7. 1 Hector Mine earthquake, California, from space geodetic observations. Geophys. Res. Lett. 28, 3063–3066.
Fattahi, H., Amelung, F., 2015. InSAR bias and uncertainty due to the systematic and stochastic tropospheric delay. J. Geophys. Res. Solid Earth 120, 8758–8773.
Fuhrmann, T., Garthwaite, M.C., 2019. Resolving three-dimensional surface motion with InSAR: Constraints from multi-geometry data fusion. Remote Sens. 11, 241. https://doi.org/10.3390/rs11030241.
Gabriel, A.K., Goldstein, R.M., Zebker, H.A., 1989. Mapping small elevation changes over large areas: Differential radar interferometry. J. Geophys. Res. Solid Earth 94, 9183. https://doi.org/10.1029/JB094iB07p09183.
Gangopadhyay, P.K., Van der Meer, F., Van Dijk, P.M., Saha, K., 2012. Use of satellite-derived emissivity to detect coalfire-related surface temperature anomalies in Jharia coalfield. India. Int. J. Remote Sens. 33, 6942–6955.
Ge, L., Chang, H.-C., Rizos, C., 2007. Mine subsidence monitoring using multi-source satellite SAR images. Photogramm. Eng. Remote Sensing. 73, 259–266.
Grohmann, C.H., 2018. Evaluation of TanDEM-X DEMs on selected Brazilian sites: Comparison with SRTM, ASTER GDEM and ALOS AW3D30. Remote Sens. Environ. 212, 121–133.
Gupta, M., Mohanty, K.K., Kumar, D., Banerjee, R., 2014. Monitoring surface elevation changes in Jharia coalfield, India using synthetic aperture radar interferometry. Environ. Earth Sci. 71, 2875–2883.
Hu, J., Li, Z.W., Ding, X.L., Zhu, J.J., Zhang, L., Sun, Q., 2014. Resolving three-dimensional surface displacements from InSAR measurements: A review. Earth-Sci. Rev. 133, 1–17.
Jevrejeva, S., Moore, J., Grinsted, A., 2003. Influence of the Arctic Oscillation and El Niño-Southern Oscillation (ENSO) on ice conditions in the Baltic Sea: The wavelet approach. J. Geophys. Res Atmospheres 108.
Jimenez-Munoz, J.C., Cristobal, J., Sobrino, J.A., Soria, G., Ninyerola, M., Pons, X., Pons, X., 2009. Revision of the single-channel algorithm for land surface temperature retrieval from Landsat thermal-infrared data. IEEE Trans. Geosci. Remote Sens. 47, 339–349.
Kuenzer, C., Stracher, G.B., 2012. Geomorphology of coal seam fires. Geomorphology 138, 209–222.
Kumar, S., Pal, S.K., 2020. Underground Coal fire Mapping Using Analysis of Self-potential (SP) Data Collected from Akashkinaree Colliery, Jharia Coalfield. India. J. Geol. Soc. India. 95, 350–358.
Liu, Y., San Liang, X., Weisberg, R.H., 2007. Rectification of the bias in the wavelet power spectrum. J. Atmos. Ocean. Technol. 24, 2093–2102.
Martha, T.R., Guha, A., Kumar, K.V., Kamaraju, M.V.V., Raju, E.V.R., 2010. Recent coal-fire and land-use status of Jharia Coalfield, India from satellite data. Int. J. Remote Sens. 31, 3243–3262.
Michalski, S.R., 2004. The Jharia mine fire control technical assistance project: An analysis. Int. J. Coal Geol. 59 (1–2), 83–90. https://doi.org/10.1016/j.coal.2003.11.005.
Mogi, K., 1958. Relations between the eruptions of various volcanoes and the deformations of the ground surfaces around them. Bull. Earthq. Res. Inst. 36, 99–134.
Okada, Y., 1985. Surface deformation due to shear and tensile faults in a half-space. Bull. Seismol. Soc. Am. 75 (4), 1135–1154.
PAL, S.K., VAISH, JITENDRA, KUMAR, SAHADEV, BHARTI, ABHAY.KUMAR., 2016. Coal fire mapping of East Basuria Colliery, Jharia coalfield using vertical derivative technique of magnetic data. J. Earth Syst. Sci. 125, 165–178.
Paul, S., Chatterjee, R., 2011. Mapping of cleats and fractures as an indicator of in-situ stress orientation, Jharia coalfield. India. Int. J. Coal Geol. 88, 113–122.
Prakash, A., Gens, R., Prasad, S., Raju, A., Gupta, R.P., 2013. Coal fires in the Jharia coalfield, India. Coal and Peat Fires: A Global Perspective. Photographs Multimedia Tours 2, 153–177.
Przyłucka, M., Herrera, G., Graniczny, M., Colombo, D., Béjar-Pizarro, M., 2015. Combination of conventional and advanced DInSAR to monitor very fast mining subsidence with TerraSAR-X data: Bytom City (Poland). Remote Sens. 7, 5300–5328.
Riyas, M.J., Syed, T.H., Kumar, H., Kuenzer, C., 2021. Detecting and Analyzing the Evolution of Subsidence Due to Coal Fires in Jharia Coalfield, India Using Sentinel-1 SAR Data. Remote Sens. 13, 1521. https://doi.org/10.3390/rs13081521.
Singh, R.P., Yadav, R.N., 1995. Prediction of subsidence due to coal mining in Raniganj coalfield, West Bengal. India. Eng. Geol. 39, 103–111.
Srivastava, V.K., Agarwal, S., Majumdar, T.J., 2017. Subsidence mapping related to coal mine fires in the Jharia coal field (India) Using Aster Tir and ERS SAR data. J. Earthq. Eng. 4, 17–34.
Tadono, T., Ishida, H., Oda, F., Naito, S., Minakawa, K., Iwamoto, H., 2014. Precise global DEM generation by ALOS PRISM. ISPRS Annals of the Photogrammetry. Remote Sens. Spatial Inf. Sci. 2, 71–76.
Takaku, J., Tadono, T., Tsutsui, K., Ichikawa, M., 2018, Quality Improvements of 'AW3D'Global Dsm Derived from Alos Prism. In IGARSS 2018-2018 IEEE International Geoscience and Remote Sens. Symposium, 1612-1615.
Torrence, C., Compo, G.P., 1998. A practical guide to wavelet analysis. Bull. Am. Meteorol. Soc. 79, 61–78.
Vaish, J., Pal, S., 2016. Subsurface Coal fire mapping of Patherdih Colliery a part of Jharia coal field. India. J. Geol. Soc. India 80–85.
Verma, R.K., Bhuin, N.C., Mukhopadhyay, M., 1979. Geology, structure and tectonics of the Jharia coalfield, India—a three-dimensional model. Geoexploration 17, 305–324.
Wan, Z., Li, Z.-L., 2008. Radiance-based validation of the V5 MODIS land-surface temperature product. Int. J. Remote Sens. 29, 5373–5395.
Liu, J., Wang, Y., Li, Y.i., Dang, L., Liu, X., Zhao, H., Yan, S., 2019a. Underground Coal Fires Identification and Monitoring Using Time-Series InSAR With Persistent and Distributed Scatterers: A Case Study of Miquan Coal Fire Zone in Xinjiang, China. IEEE Access 7, 164492–164506.
Wang, T., Shi, J., Ma, Y.a., Husi, L., Comyn-Platt, E., Ji, D., Zhao, T., Xiong, C., 2019b. Recovering land surface temperature under cloudy skies considering the solar-cloud-satellite geometry: application to MODIS and Landsat-8 data. J. Geophys. Res. Atmospheres 124, 3401–3416.
Yun, H.-W., Kim, J.-R., Yoon, HaSu, Choi, YunSoo, Yu, JungHum, 2019. Seismic Surface Deformation Risks in Industrial Hubs: A Case Study from Ulsan, Korea, Using DInSAR Time Series Analysis. Remote Sens. 11, 1199.
Yunjun, Z., Fattahi, H., Amelung, F., 2019. Small baseline InSAR time series analysis: Unwrapping error correction and noise reduction. Comput. Geosci. 133, 104331.